

# In situ TEM revealing pretreatment and interface effects in $\text{Ge}_2\text{Sb}_2\text{Te}_5$

HPSTAR  
1018-2020Cite as: Appl. Phys. Lett. **116**, 222105 (2020); doi: 10.1063/5.0007124

Submitted: 9 March 2020 · Accepted: 26 May 2020 ·

Published Online: 4 June 2020



View Online



Export Citation



CrossMark

Ruiwen Shao,<sup>1</sup> Lihua Wang,<sup>2</sup>  Weikang Dong,<sup>1,3</sup> Lixin Yao,<sup>4</sup> Yongjin Chen,<sup>5</sup> Lixin Dong,<sup>6</sup> Kun Zheng,<sup>2,a)</sup>   
and Xiaodong Han<sup>2,a)</sup>

## AFFILIATIONS

<sup>1</sup>Beijing Advanced Innovation Center for Intelligent Robots and Systems, Institute of Convergence in Medicine and Engineering, Beijing Institute of Technology, Beijing 100081, China<sup>2</sup>Beijing Key Lab of Microstructure and Property of Solids, Institute of Microstructure and Properties of Advanced Materials, Beijing University of Technology, Beijing 100124, China<sup>3</sup>Analysis and Testing Center, Beijing Institute of Technology, Beijing 100081, China<sup>4</sup>College of Mechatronic Engineering, North University of China, Taiyuan 038507, China<sup>5</sup>Center for High Pressure Science and Technology Advanced Research, Beijing 100094, China<sup>6</sup>Department of Biomedical Engineering, City University of Hong Kong, Tat Chee Avenue, Kowloon Tong, Hong Kong<sup>a)</sup>Authors to whom correspondence should be addressed: [kunzheng@bjut.edu.cn](mailto:kunzheng@bjut.edu.cn) and [xdhan@bjut.edu.cn](mailto:xdhan@bjut.edu.cn)

## ABSTRACT

Random access memory devices that rely on phase changes are primarily limited by the speed of crystallization. However, imaging structural dynamics in working devices with nanoscale resolution remains elusive. Using an ultrafast liquid-quenching system in transmission electron microscope, we obtain a melt-quenched amorphous phase-change material  $\text{Ge}_2\text{Sb}_2\text{Te}_5$  nanosheet. We find that the applied incubation field (pretreatment) leads to nonuniform nucleus formation and growth in the amorphous  $\text{Ge}_2\text{Sb}_2\text{Te}_5$ , accompanied by a slight change in electric properties. Moreover, the phase-change mechanism changes from the material inherent crystallization mechanism (nucleation-dominated) to the heterocrystallization mechanism, indicating the incubation period of nucleation might be bypassed.

Published under license by AIP Publishing. <https://doi.org/10.1063/5.0007124>

Nonvolatile phase-change random-access memory (PCRAM) represents one of the best candidates for next-generation electronic memory hierarchy.<sup>1–5</sup> Bit storage in PCRAM cell operation relies on the reversible crystalline (c) to amorphous (a) transition of a phase-change (PC) material.<sup>2,6</sup> To achieve “universal memory” with PCRAM, subnanosecond operation is needed to compete with cache-type static random-access memory (SRAM).<sup>6</sup> Commercialized PCRAM products are limited by the tens of nanoseconds writing speed, originating from the stochastic crystal nucleation during the crystallization of amorphous  $\text{Ge}_2\text{Sb}_2\text{Te}_5$  (GST). In nucleation-driven PC materials (GST), crystallization occurs via the stochastic formation of critical nuclei and their subsequent growth. A long incubation period is needed before the critical nucleus is obtained due to the high frequency of formation and dissolution of crystalline precursors.<sup>7,8</sup>

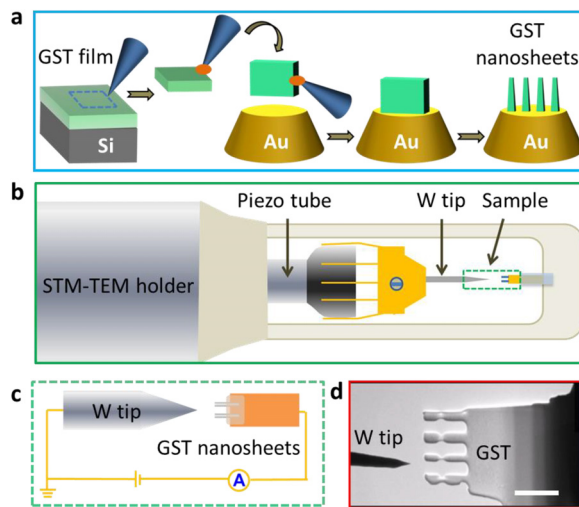
Several important strategies have been tried to improve the SET or writing speed of the current GST-based PCRAM devices by shortening the incubation period during nucleation. (i) Doping. A promising approach is doping phase-change materials with

transition metals like Sc or Ti to generate stable crystalline precursors in the amorphous matrix shortening the incubation period.<sup>3,9</sup> (ii) Incubation (pretreatment) effect. Loke *et al.* introduced a pretreatment to preseed nuclei inside the amorphous matrix, such that the ensuing SET operation becomes primary crystal growth. A very fast SET speed of  $\sim 500$  ps was achieved on an  $\sim 30$ -nm pore-like GST-based PCRAM device with the aid of a constant low voltage.<sup>10</sup> (iii) Interface effect. Improvements in crystallization speed can also be obtained by taking advantage of interface-assisted crystal growth, allowing us to bypass the incubation period during nucleation.<sup>2</sup> It was shown that the growth speed of GST could reach 1 m/s at elevated temperatures by flash differential scanning calorimetry experiments,<sup>11</sup> which is corroborated by a clear crystallization simulation study demonstrating that rapid growth from the boundaries could speed up the crystallization process.<sup>8</sup> However, direct evidence is still lacking. Thus, understanding the microscopic origin of crystallization kinetics with the aim of improving the SET speed is a major goal in the field.

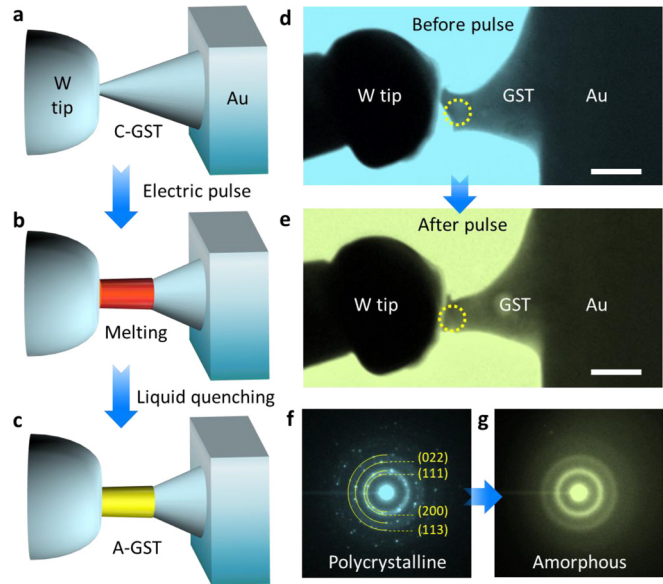
Here, we present our direct observation of the effects of the pretreatment electric field and the c–a interface on the GST nanosheet during the electric field-induced crystallization process. By building an *in situ* Joule heating nanodevice inside a TEM, we developed an ultrafast liquid-quenching system to obtain melt-quenched a-GST. We provided overwhelming evidence that at the nanometer length scale, the phase-change mechanism changes from the material inherent crystallization mechanism (nucleation-dominated) to the heterocrystallization mechanism, indicating that the incubation period during nucleation might be bypassed. The distribution of the pretreatment-induced nucleus formation and growth is nonuniform and the change in electric properties is slight, indicating that through careful design, both fast speed and stability of the amorphous phase can be achieved simultaneously.

Figure 1 schematically illustrates the preparation of TEM specimens and the setup for the *in situ* TEM experiments. TEM specimens are prepared using the focused ion beam (FIB) technique [Fig. 1(a)]. Figure 1(b) shows the *in situ* TEM experimental setup, in which the Au wire with the TEM specimen is inserted into the fixed terminal of the holder and a tungsten (W) probe is connected with the movable terminal. Before each *in situ* experiment, a large current is introduced to the tungsten tip to remove the oxide layer on its surface due to the Joule heating effect.<sup>12–14</sup>

The entire experiment involves two processes: obtaining the melt-quenched a-GST and *in situ* TEM characterization of the recrystallization of the a-GST nanosheet. Our ultrafast melt-quenching technique is illustrated in Figs. 2(a)–2(c). The “amorphization” process of GST requires that the temperature within the memory cell is higher than the melting temperature of the PC material. As the molten PC material is quenched rapidly to a lower temperature, the atomic configurations are frozen into the less-ordered amorphous state.<sup>15</sup> To obtain the melt-quenched a-GST, the W tip is first brought into contact with the GST nanosheet [Fig. 2(a)] inside the TEM. A short square



**FIG. 1.** Schematic diagrams of the experimental setup and process. (a) The FIB lift-off process. (b) The *in situ* TEM experimental setup. (c) Enlarged schematic diagram of the dashed area in panel (b). (d) Low-mag TEM image of the *in situ* TEM experimental setup and the GST samples. Scale bars: 1  $\mu\text{m}$ .



**FIG. 2.** Electric pulse-induced structural transition of crystalline-to-amorphous states. (a)–(c) Schematic drawing of the experimental configuration. The W tip is brought into contact with the GST nanosheet (a) and c-GST at the tip of the nanosheet melted by the application of a short square electric pulse (b). Heat dissipates rapidly through the W tip and Au electrode, vitrifying the melting zone to form a-GST (c). (d) and (f) TEM image of a polycrystalline state GST nanosheet and the corresponding SAED pattern. (e) and (g) TEM image of an amorphous state GST nanosheet after applying the electric pulse and the corresponding SAED pattern. Scale bars: 200 nm.

electric pulse then imposes local Joule heating on the GST nanosheet to induce the formation of a melting zone in the tip of the GST nanosheet [Fig. 2(b)]. On instantaneous cessation of the electric pulse and, consequently, local Joule heating, heat dissipates rapidly through the W tip and the conductive heat reservoir, creating an extremely high cooling rate sufficient to vitrify the melt into the amorphous state [Fig. 2(c)]. Figures 2(d) and 2(e) show a typical example showing the amorphization process of a GST nanosheet induced by an electric pulse. Figures 2(f) and 2(g) show the selected area electron diffraction (SAED) patterns corresponding to the GST nanosheet before and after the electric pulse, from which the a-GST nanosheet can be confirmed after the electric pulse. A distinct interface is observed between the a-GST and c-GST (supplementary material Fig. S1). This a-GST TEM specimen can serve as an ideal platform to study the microstructural evolution during the recrystallization process.

To investigate the pretreatment effect, the electrical measurements and TEM characterization are carried out simultaneously with the melt-quenched a-GST nanosheet. Figure 3(a) shows three dark field (DF) TEM images of a section of the GST nanosheet captured when a pretreatment electric field is applied. No crystalline state GST grains are observed in the a-GST (image 1 and supplementary material Fig. S1). Then, a DC voltage (pretreatment electric field) is applied with an increased interval of 20 mV and a dwell time of 10 s. With the increasing pretreatment voltage, the current increases gradually [Fig. 3(b)]. This observed nonlinear  $I$ – $V$  characteristic can be attributed to the typical conduction behavior of a-GST, which follows the Poole–Frenkel

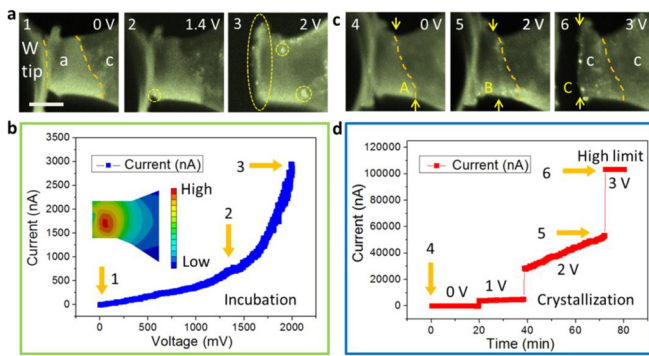


**FIG. 3.** The microstructural evolution of the melt-quenched a-GST with the measured electric properties. (a) DF TEM images of the a-GST nanosheet showing microstructural evolution during the application of the pretreatment electric field with images (1) 0 V, (2) 1.4 V, and (3) 2 V. In image 3, the W tip is moved away and then moved back after careful TEM characterization. (b) The relationship between the voltage applied and current through the GST nanosheet. The inset shows a two-dimensional finite element analysis of the temperature distribution. (c) The microstructural evolution of a-GST (after pretreatment) during the application of crystallization voltages with images (4) 0 V, (5) 2 V, and (6) 3 V. The W tip is moved away again in image 6. (d) The relationship between the voltage applied and current corresponding to the subsequent crystallization process. Note that the current in image 6 reaches the high limit of the measurement. Scale bars: 100 nm.

(PF) conduction mechanism.<sup>16</sup> The underlying mechanism is commonly related to the field-induced increase in the carrier concentration.<sup>17</sup> Orange arrows in Fig. 3(b) are indicated corresponding to the three DF TEM images in Fig. 3(a). No obvious changes are observed in the a-GST specimen before the pretreatment voltage reaches 1.4 V. When the voltage reaches 1.4 V, a grain with a size of about 4 nm appears at the tip of the GST [image 2 in Fig. 3(a)]. Figure S2 shows chronologically enlarged DF TEM images of the nucleation and growth process of another grain. When the voltage is increased to 2 V, several grains emerge [image 3 in Fig. 3(a)]. Finally, the pretreatment voltage is reduced to 0 V. For as-deposited a-GST, no visible structural changes are observed during the application of the pretreatment electric field (supplementary material Fig. S3), consistent with the *ex situ* experiments.<sup>18–21</sup>

It should be noted that most of the crystalline grains are distributed around the two interfaces [indicated by yellow dashed circles in Fig. 3(a) image 3]. The sandwiched zone between the tungsten tip and the crystalline GST remains amorphous. This nonuniform distribution may be due to the interface effect or Joule heating-induced temperature distribution. To better understand the nucleation kinetics of the a-GST, a two-dimensional finite element analysis is applied to simulate the temperature distribution during the incubation process, as shown in the inset in Fig. 3(b). The heat generated by the current pulse is concentrated in the active phase-change area. Compared to the middle area of the a-GST, the temperature near the tungsten electrode is lower. This inconsistency suggests that the nonuniform distribution might be a result of the smaller activation energy of crystallization at the interface rather than the temperature distribution. These results agree with previous reports that the heterogeneous nucleation rates are observed to be far higher than the homogeneous nucleation rates.<sup>22,23</sup>

Following the completion of the above pretreatment process, another DC voltage (crystallization voltage) with an increased interval

of 1 V is applied [Fig. 3(c)]. Surprisingly, when the voltage is increased to 2 V, crystal growth-induced partial crystallization from the c-a interface (heterogeneous crystallization) occurs [image 5 in Fig. 3(c)]. The c-a interface moves from position A to position B, accompanied by the linear increment of the current through the GST nanosheet [Fig. 3(d)]. This partial crystallization mechanism is quite different from the traditional homogeneous crystallization. However, when the voltage is increased to 3 V, a homogeneous crystallization within the a-GST matrix occurs (image 6). The observation of randomly oriented nanosized grains is consistent with the well-established homogeneous nucleation-dominated phase-change mechanism of GST. Altogether, we provide direct evidence for the proposal that the recrystallization of amorphous nucleation-dominated GST occurs both from the interface and within the interior. Moreover, heterogeneous crystallization occurs at 2 V, in contrast to the homogeneous nucleation and growth occurring at 3 V, confirming that the activation energy of crystallization at the interface is smaller. More details about the heterogeneous crystallization (2 V) and subsequent homogeneous crystallization (3 V) processes are shown in Fig. S4.

It is worth mentioning that the current at 2 V voltage increases to about 30 000 nA [Fig. 3(d)], much larger than the current with the same voltage at the end point of the pretreatment process [about 3000 nA, Fig. 3(b)]. This discrepancy could be attributed to continuous Joule heating and the percolation phenomenon, in which enhanced electrical conduction is not observed until the crystal grains are connected to each other, forming a continuous electrical path.<sup>10,24</sup> The other thing that should be mentioned is that the crystallization voltage (2 V) applied in this experiment is much lower than the voltage in our previous experiment using as-deposited a-GST.<sup>25</sup> Many studies have demonstrated that the a-GST nanosheets show different resistances and microstructures corresponding to the as-deposited and the melt-quenched state.<sup>24,26–28</sup>

The electric properties corresponding to the a-GST before and after pretreatment and crystalline states are also determined (Fig. 4). The resistance of the GST nanosheet is measured by applying a voltage, swept from 0 to 200 mV. The insets show corresponding images and schematics of the microstructure of the three types of GST states. The red curve shows the initial transport properties of the melt-quenched high-resistance amorphous state before pretreatment. After the pretreatment process, a number of nuclei appear in the a-GST nanosheet. The conductance measured for this amorphous state GST after pretreatment (blue curve) is  $\sim 3$  times higher when compared to

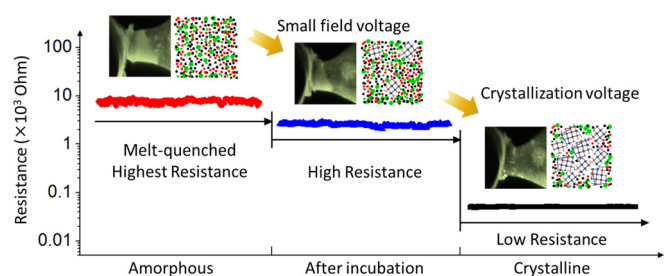


**FIG. 4.** Electric properties corresponding to the amorphous (before/after pretreatment) and crystalline states. The insets show the DF TEM images and corresponding schematics of the three-state GST.

the amorphous case before pretreatment (red curve). When the crystallization voltage is applied, the film is transformed from the amorphous state into a low resistance polycrystalline state. The conductance measured for the crystalline state GST (dark curve) is two orders of magnitude larger when compared to the amorphous case before pretreatment (red curve). Based on these results, we can conclude that the change in electric properties induced by the pretreatment electric field (blue curve) is slight compared to the crystalline state (dark curve), indicating that through careful design of the PCRAM device, both fast speed and stability of the amorphous phase can be achieved simultaneously.

A previous study has demonstrated that the pretreatment process can substantially promote the nucleation and growth of PC materials via prestructural ordering effects,<sup>10</sup> indicating the presence of microstructural variations in the amorphous material. In this study, we find that the applied pretreatment electric field leads to the nonuniform formation and growth of nuclei in a-GST, thus speeding up the crystallization process, accompanied by a slight change in electric properties. Most nuclei are distributed around the interfaces because of the smaller activation energy of crystallization at the interfaces. Therefore, they could accelerate its phase-switching speeds, without harming the long-term stability of the switched state. Another important finding in our experiment is that a heterogeneous crystallization at the c-a interface was observed. At the nanometer length scale, the heterogeneous crystallization at the interface starts to prevail, consistent with first-principles calculations.<sup>7,8</sup> The heterogeneous crystallization starts with lower current and temperature (2 V) compared to the homogeneous nucleation (3 V), indicating that the heterogeneous crystallization activation energy at the interface is smaller compared to homogeneous nucleation, in accordance with the previous results.<sup>22,23,29</sup> This result indicates that the heterogeneous crystallization rate will become the dominant mechanism when the size of the memory cell decreases further. In addition, it has been reported that electron beam-induced crystallization has been observed consistently in PCRAMs.<sup>30–32</sup> By reducing the beam intensity, crystallization was effectively prohibited. For example, no obvious change in a-GST could be observed in JEOL JEM-2100F TEM with the beam intensity lower than  $1.6 \times 10^{23} \text{ em}^{-2} \text{ s}^{-1}$  within 90 min.<sup>33</sup> In our experiment, the dose rate (DF image mode) was kept at  $2.1 \text{ pA/cm}^2$  ( $1.3 \times 10^{11} \text{ em}^{-2} \text{ s}^{-1}$ ), which is a relatively low dose for TEM observation. Therefore, the influence of the electron irradiation in our experiment is small.

In conclusion, by combining the TEM characterization and electrical measurements of the GST nanosheet, we determine the effect of the interface and pretreatment electric field on the structural transformations of the GST nanosheet. We find that the pretreatment leads to the formation and growth of nuclei in a-GST, which can induce faster crystallization. Besides, we provide overwhelming evidence for the proposal that the heterogeneous crystallization occurs as well as homogenous crystallization in the crystallization process of GST, suggesting that the interface plays a critical role in achieving the desired crystallization characteristics.

See the [supplementary material](#) for the experiment and methods, DF TEM images of the a-GST and c-GST, nucleation and growth process of another grain, pretreatment process of the as-deposited a-GST, and heterogeneous crystallization process of the melt-quenched a-GST.

This work was supported by the National Key Research and Development Project (No. 2018YFB1304902), the National Natural Science Foundation of China (Nos. 11904372, 91860202, 11774016, 11704389, and U1813211), the Beijing Natural Science Foundation (No. Z180014), the “111” project (No. DB18015), the Beijing Institute of Technology Research Fund Program for Young Scholars, the Beijing Institute of Technology Laboratory Research Project (No. 2019BITSYA03), and the Beijing Outstanding Young Scientists Projects (Nos. BJJWZYJH01201910005018 and BJJWZYJH01201910005018).

## DATA AVAILABILITY

The data that support the findings of this study are available from the corresponding author upon reasonable request.

## REFERENCES

- <sup>1</sup>K. Ding, J. Wang, Y. Zhou, H. Tian, L. Lu, R. Mazzarello, C. Jia, W. Zhang, F. Rao, and E. Ma, *Science* **366**, 210 (2019).
- <sup>2</sup>W. Zhang, R. Mazzarello, M. Wuttig, and E. Ma, *Nat. Rev. Mater.* **4**, 150 (2019).
- <sup>3</sup>F. Rao, K. Ding, Y. Zhou, Y. Zheng, M. Xia, S. Lv, Z. Song, S. Feng, I. Ronneberger, R. Mazzarello, W. Zhang, and E. Ma, *Science* **358**, 1423 (2017).
- <sup>4</sup>S. Nam, H. Chung, Y. C. Lo, L. Qi, J. Li, Y. Lu, A. T. C. Johnson, Y. Jung, P. Nukala, and R. Agarwal, *Science* **336**, 1561 (2012).
- <sup>5</sup>F. Xiong, A. D. Liao, D. Estrada, and E. Pop, *Science* **332**, 568 (2011).
- <sup>6</sup>H. S. P. Wong and S. Salahuddin, *Nat. Nanotechnol.* **10**, 191 (2015).
- <sup>7</sup>J. Akola, R. O. Jones, and J. Kalikka, *Phys. Rev. B* **90**, 184109 (2014).
- <sup>8</sup>I. Ronneberger, W. Zhang, H. Eshet, and R. Mazzarello, *Adv. Funct. Mater.* **25**, 6407 (2015).
- <sup>9</sup>M. Zhu, M. Xia, F. Rao, X. Li, L. Wu, X. Ji, S. Lv, Z. Song, S. Feng, and H. Sun, *Nat. Commun.* **5**, 4086 (2014).
- <sup>10</sup>D. Loke, T. H. Lee, W. J. Wang, L. P. Shi, R. Zhao, Y. C. Yeo, T. C. Chong, and S. R. Elliott, *Science* **336**, 1566 (2012).
- <sup>11</sup>J. Orava, A. L. Greer, B. Gholipour, D. W. Hewak, and C. E. Smith, *Nat. Mater.* **11**, 279 (2012).
- <sup>12</sup>K. Zheng, Z. Zhang, Y. Hu, P. Chen, W. Lu, J. Drennan, X. Han, and J. Zou, *Nano Lett.* **16**, 1787 (2016).
- <sup>13</sup>K. Zheng, R. Shao, J. Wang, Z. Liao, N. Marks, P. Chen, W. Lu, X. Han, and J. Zou, *Carbon* **100**, 435 (2016).
- <sup>14</sup>R. W. Shao, K. Zheng, B. Wei, Y. F. Zhang, Y. J. Li, X. D. Han, Z. Zhang, and J. Zou, *Nanoscale* **6**, 4936 (2014).
- <sup>15</sup>L. Zhong, J. Wang, H. Sheng, Z. Zhang, and S. X. Mao, *Nature* **512**, 177 (2014).
- <sup>16</sup>M. Nardone, M. Simon, I. V. Karpov, and V. G. Karpov, *J. Appl. Phys.* **112**, 071101 (2012).
- <sup>17</sup>D. Ielmini and Y. Zhang, *J. Appl. Phys.* **102**, 054517 (2007).
- <sup>18</sup>B. S. Lee, G. W. Burr, R. M. Shelby, S. Raoux, C. T. Rettner, S. N. Bogle, K. Darmawikarta, S. G. Bishop, and J. R. Abelson, *Science* **326**, 980 (2009).
- <sup>19</sup>B. S. Lee, K. Darmawikarta, S. Raoux, Y. H. Shih, Y. Zhu, S. G. Bishop, and J. R. Abelson, *Appl. Phys. Lett.* **104**, 071907 (2014).
- <sup>20</sup>M. Naito, M. Ishimaru, Y. Hirotsu, and M. Takashima, *J. Appl. Phys.* **95**, 8130 (2004).
- <sup>21</sup>V. Weidenhof, I. Friedrich, S. Ziegler, and M. Wuttig, *J. Appl. Phys.* **89**, 3168 (2001).
- <sup>22</sup>W. Zhang, I. Ronneberger, P. Zalden, M. Xu, M. Salinga, M. Wuttig, and R. Mazzarello, *Sci. Rep.* **4**, 6529 (2014).
- <sup>23</sup>K. F. Kelton, *Solid State Phys.* **45**, 75 (1991).
- <sup>24</sup>B. S. Lee, R. M. Shelby, S. Raoux, C. T. Rettner, G. W. Burr, S. N. Bogle, K. Darmawikarta, S. G. Bishop, and J. R. Abelson, *J. Appl. Phys.* **115**, 063506 (2014).
- <sup>25</sup>R. Shao, K. Zheng, Y. Chen, B. Zhang, Q. Deng, L. Jiao, Z. Liao, Z. Zhang, J. Zou, and X. Han, *J. Mater. Chem. C* **4**, 9303 (2016).

- <sup>26</sup>J. Park, M. Kim, W. Choi, H. Seo, and C. Yeon, *Jpn J. Appl. Phys., Part 1* **38**, 4775 (1999).
- <sup>27</sup>P. K. Khulbe, E. M. Wright, and M. Mansuripur, *J. Appl. Phys.* **88**, 3926 (2000).
- <sup>28</sup>M. S. Youm, Y. T. Kim, and Y. S. Man, *Appl. Phys. Lett.* **91**, 083508 (2007).
- <sup>29</sup>J. A. Kalb, F. Spaepen, and M. Wuttig, *J. Appl. Phys.* **98**, 43 (2005).
- <sup>30</sup>T. Jiang, J. Wang, L. Lu, C. Ma, D. Zhang, F. Rao, C. Jia, and W. Zhang, *APL Mater.* **7**, 81121 (2019).
- <sup>31</sup>T. Jiang, X. Wang, J. Wang, Y. Zhou, D. Zhang, L. Lu, C. Jia, M. Wuttig, R. Mazzeo, and W. Zhang, *Acta Mater.* **187**, 103 (2020).
- <sup>32</sup>B. J. Kooi and J. T. M. De Hosson, *J. Appl. Phys.* **92**, 3584 (2002).
- <sup>33</sup>J. Wang, T. Jiang, L. Tian, D. Zhang, and W. Zhang, *Mater. China* **38**, 110 (2019).